



OPEN

Radial-tangential mode of single-wall carbon nanotubes manifested by Landau regulation: reinterpretation of low- and intermediate-frequency Raman signals

K. P. S. S. Hembram¹, Jin-Gyu Kim², Sang-Gil Lee², Jeongwon Park^{3,4} & Jae-Kap Lee^{1✉}

The low-frequency Raman signals of single-wall carbon nanotubes (SWNTs), appearing in the range of 100–300 cm^{-1} , have been interpreted as radial-breathing mode (RBM) comprising pure radial Eigenvectors. Here, we report that most of the low-frequency and intermediate-frequency signals of SWNTs are radial-tangential modes (RTMs) coexisting radial and tangential Eigenvectors, while only the first peak at the low-frequency side is the RBM. Density functional theory simulation for SWNTs of ~ 2 nm in diameter shows that dozens of RTMs exhibit following the RBM ($\sim 150 \text{ cm}^{-1}$) up to G -mode ($\sim 1592 \text{ cm}^{-1}$) in order with Landau regulation. We specify the RBM and the RTM on Raman spectra obtained from SWNTs, where both appear as prominent peaks between 149 and 170 cm^{-1} and ripple-like peaks between 166 and 1440 cm^{-1} , respectively. We report that the RTMs have been regarded as RBM ($\sim 300 \text{ cm}^{-1}$) and ambiguously named as intermediate-frequency mode (300–1300 cm^{-1}) without assignment. The RTMs gradually interlink the RBM and the G -mode resulting in the symmetric Raman spectra in intensity. We reveal high-resolution transmission microscope evidence for a helical structure of SWNTs, informing the typical diameter of commercial SWNTs to be 1.4–2 nm.

Raman spectra of single-wall carbon nanotubes (SWNT)¹ exhibit the tangential G -mode at $\sim 1592 \text{ cm}^{-1}$ (including G' peak at 1572 cm^{-1}) and the non-tangential low-frequency signals at 100–300 cm^{-1} , together with the defect-related D band at $\sim 1350 \text{ cm}^{-1}$. The low-frequency signals have been interpreted as radial-breathing mode (RBM)², which is regarded as an important indicator of discerning diameters as well as electronic properties of SWNTs^{1–6}. This is due to the general understanding that it originated with synchronous radial vibration of the carbon atoms^{2,3} in tubular graphene to be correlated with their diameters, affecting, in turn, their chirality⁷. The RBM mostly appears as a band comprising multiple peaks, and this band signal has been attributed to the presence of plural SWNTs with different diameters to be ~ 0.5 –2 nm for 100–300 cm^{-1} from the equation, $\omega_{\text{RBM}} (\text{cm}^{-1}) = \sim 248/d$ where d is diameters of SWNTs^{3–5}.

The low-frequency Raman signals have also been observed from graphene (or nano-graphitic) structures^{8–16}. This is unexpected because they are considered unique to SWNTs, *i.e.*, tubular graphene. Thus some researchers name the low-frequency Raman signals of the graphene structures as RBM-like without further explanation^{11,15} or layer breathing modes of bilayer graphene^{13,14}. Lee et al. have shown that the low-frequency Raman signals of graphene structures (100–500 cm^{-1}) are due to the radial mode (RM) formed by end nano-curvatures of mono- or bilayer graphene¹⁶. Indeed, the limit of the low-frequency Raman signals of SWNTs has been inconsistently reported to be ~ 200 , ~ 250 , ~ 300 , ~ 350 , and $\sim 400 \text{ cm}^{-1}$, while some well-defined Raman spectra of SWNTs reveal many ripple-like peaks^{1–5,17–27} distributed from $\sim 200 \text{ cm}^{-1}$ to $\sim 1300 \text{ cm}^{-1}$. Those appearing between ~ 600

¹Center for Opto-Electronic Materials and Devices, Korea Institute of Science and Technology (KIST), Seoul 02792, Republic of Korea. ²Center for Research Equipment, Korea Basic Science Institute, Daejeon 34133, Republic of Korea. ³Department of Electrical and Biomedical Engineering, University of Nevada, Reno, NV 89557, USA. ⁴School of Electrical Engineering and Computer Science, University of Ottawa, Ottawa, ON K1N 6N5, Canada. ✉email: jklee@kist.re.kr

and $\sim 1300\text{ cm}^{-1}$ have been generally named as intermediate-frequency modes (IFM)^{1,2,18,19,23–27} without assignment or overlooked^{3–5,21,22}. This IFM naming (which means ‘unassigned’) left another issue, the unclear boundary between RBMs and IFMs. Also, the calculated diameters of 0.5–2.0 nm for 100–500 cm^{-1} are too small, compared with 1.4–2 nm of SWNTs directly observed by HRTEM^{21,28–33}. These indicate that the nature of the vibrational modes still puzzles in spite of numerous investigations for the different graphene structures.

Recently, there has been an issue with the structure of SWNTs, *i.e.*, to be non-tubular (helical) morphology, which is contrary to the conventional tube model (Supplementary Fig. 1). High-resolution transmission microscope (HRTEM)^{28–33} and scanning tunneling microscope (STM)^{34,35} images where traces of graphene helix are evident (Supplementary Fig. 2), energy calculation²⁸, as well as direct field emission microscopy observation where the turning (*i.e.*, helical) growth of SWNTs³⁶ have all been used to support the helix model. However, these evidences for helical SWNTs have yet to be noticed or overlooked with the chiral theory⁷, which not only provides theoretical background of the tube model but also justifies the diverse electronic features^{6,23}, conducting or semiconducting with a different band gap of SWNTs reported³⁵.

Park et al. have reinterpreted SWNTs as a graphene helix with the Raman study, including simulations for different (concentric and opened) SWNT structures³⁷. They have shown that the *G* peak ($\sim 1575\text{ cm}^{-1}$) unique to SWNTs is the characteristic of their helical structure, reporting the radial-tangential modes (RTMs) assigned as the shoulder peak ($\sim 186\text{ cm}^{-1}$) of the RBM. In this article, we explore vibrational features for concentric and opened (helical) tube structures as well as curved graphene with first-principles calculation and measurement and show that RBM, RTM, and *G*-mode are governed by Landau regulation.

Results and discussion

TEM and Raman analysis. Figure 1 shows TEM images for Tuball-SWNTs. They appear as a bundle of tens of nm in diameter with a metal catalyst (white arrow in Fig. 1a), which is the same as those for the samples reported by others³⁷. Diameters are measured to be ~ 1.4 –2.0 nm, similar to those of the arc-SWNT samples²⁸ (Fig. 1b), and some samples reveal helical traces indicated by the yellow arrows.

Raman spectra obtained from the two kinds of samples reveal the low-frequency band of 100–200 cm^{-1} (inset), the *D* band at $\sim 1350\text{ cm}^{-1}$, and the strong tangential *G* band at $\sim 1590\text{ cm}^{-1}$, as shown in Fig. 2a, which are typical to SWNTs^{1–5}. Arc-SWNTs reveal a strong peak at 169 cm^{-1} and its shoulder peak at 188 cm^{-1} , while Tuball-SWNTs reveal a strong peak at 149 cm^{-1} and a few peaks at 120 cm^{-1} , 137 cm^{-1} , and 166 cm^{-1} . Both samples reveal many weak but clear signals at ~ 200 –1500 cm^{-1} , as shown in their magnified Raman spectra (Fig. 2b). We assign these ripple-like peaks to the RTMs where low nodes (1st, 2nd, and 3rd) peaks are specified with the simulated Raman modes for concentric and opened tube structures shown in Fig. 3.

Raman simulation. The RBM, where all Eigenvectors are directed towards the center of the axis, is evident in the 0th node of the concentric tube (Figs. 3b and c). The 0th node for the opened tube (helical geometry) and curved graphene reveals localized RBM (*l*-RBM) where the radial Eigenvectors are localized (Fig. 3d–f) compared with that of RBM. RTMs, featured by a mixture of localized radial mode (*l*-RM) and tangential mode (*l*-TM) Eigenvectors, reveal two degenerated or non-degenerated frequencies per node in between RBM and *G*-mode (Supplementary Fig. 3). The total number of RTMs (N_{RTM}) for the concentric tube is $2n$ where n is the number of nodes, and ‘2’ represents two modes per node. Two modes in each node for the concentric tube are degenerate, while those for the opened tube are non-degenerate. We attribute the non-degeneracy, the appearance of the *l*-RBM (or *l*-RM), and the lack of one 1st node RTM for the opened tube, to their structural asymmetry (Fig. 3d and e).

The locally distorted opened SWNT structure reveals relatively strong *l*-RMs on the steep edge curvature at higher nodes up to the 4th (Supplementary Fig. 3). Frequencies of RBMs (*l*-RBM) and RTMs for SWNTs depend on their diameters as well as local curvatures. With an increase of nodes, the frequencies of RTMs monotonically increase, and the *l*-RMs become weaker. The simulation data indicates that the *G*-mode and the RBM are both extreme Raman modes comprising pure RM and pure TM Eigenvectors, respectively, with an energy state (Fig. 3).

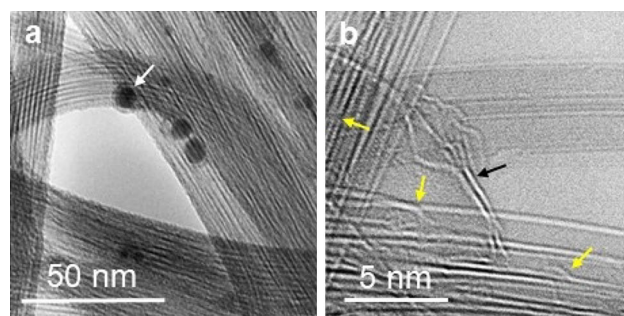


Figure 1. TEM images for Tuball-SWNTs. (a) Low magnification. (b) HRTEM. The samples coexist with metal catalysts (white arrow in (a)) as well as graphitic structures (black arrow in (b)).

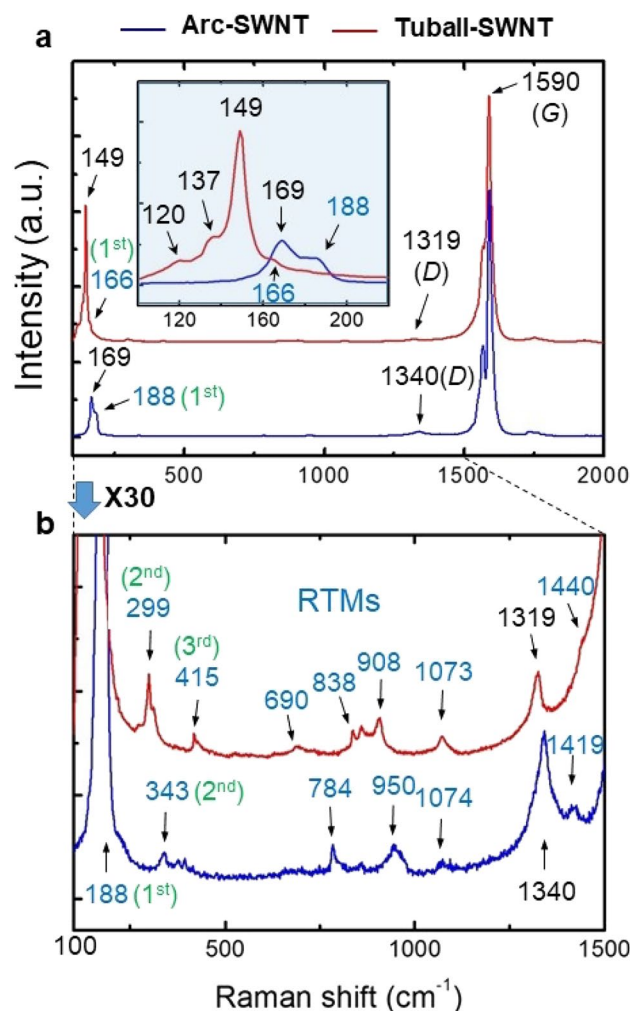


Figure 2. Raman spectra of SWNT samples. (a) Raman spectra obtained from purified and bundled Tuball- and arc-SWNTs samples revealing typical Raman signals for SWNTs. Inset in (a) shows a zoom-in view of the low-frequency range. (b) Zoom-in view of the spectra of (a).

Landau regulation of Raman modes. We see the *l*-RM and the *l*-TM comprising the RTMs to two different phases in a phase diagram of a material where Landau theory works³⁹. This enables us to clarify the simulation data shown in Fig. 3 with Landau free energy formula, $f(\delta) = f_0(\delta) + \alpha(\delta - \delta_c)m^2 + 1/2\beta m^4$, $\alpha > 0$, $\beta > 0$, where $f(\delta)$ is the free energy functional, δ is the infinitesimal displacement of atoms (Fig. 3h and i), m is the order parameter, α and β are parameters. When $\delta > \delta_c$, the phase has one energy state revealing one minimum (RBM or G-mode, *i.e.*, all atoms in the wall of SWNTs have a synchronous radial or tangential vibration, respectively) (Fig. 3a), while the phase has two energy states revealing two minima (RTM) (Fig. 3a') when $\delta < \delta_c$.

Figure 4 elucidates 1st and 2nd node RTMs featured by *l*-RMs and *l*-TMs. Both RTMs reveal two and four decentered focuses, respectively (red dots in Fig. 4a and b). Figure 4a' and b' depict the spatial variation of Eigenvectors, which is represented by a sine curve, $A_0 \sin(\omega t + \varphi)$, where A_0 is the amplitude, $\omega = 2\pi f$ (f is the angular frequency of oscillation), t is the time period, and φ is the phase (Fig. 4a' and b'). The sine curve is regulated by the coherence length (ξ), a cycle of TM-RM-TM-RM-TM variation (the distance moved by the wave per one oscillation), which is described as $2\pi r/n$ where r and n are a radius of the tubular structures and a number of nodes, respectively. With an increase in nodes, the coherence length, which is an intrinsic characteristic of the geometry, shortens, and the amplitude (A) of the sine curve (corresponding to pure radial components of *l*-RMs) decreases. The depth of focus (d_f) of the *l*-RMs (Fig. 4a) also decreases with the nodes, as shown in Fig. 5. This indicates that the coherence length, the amplitude as well as the depth of focus (d_f) can be indicators to estimate the intensity of the RTMs.

With the simulation data and their analysis (Figs. 3, 4, 5), we assign the strong peak at 169 cm^{-1} and its shoulder peak at 188 cm^{-1} for arc-SWNTs (Fig. 2) to the RBM (*l*-RBM) and the 1st node RTM, respectively. For Tuball-SWNTs, we assign 149 cm^{-1} and $\sim 166 \text{ cm}^{-1}$ peaks to RBM (*l*-RBM) and 1st node RTM respectively. We also assign many signals below $\sim 500 \text{ cm}^{-1}$ in the zoom-in spectra (Fig. 2b) to RTMs, 299 and 415 cm^{-1} peaks of Tuball-SWNTs to the 2nd and the 3rd node RTMs respectively, 343 cm^{-1} peak of Arc-SWNTs to the 2nd node RTM. On the other hand, we could not assign the higher-frequency RTMs at 600–1500 cm^{-1} . With the variation

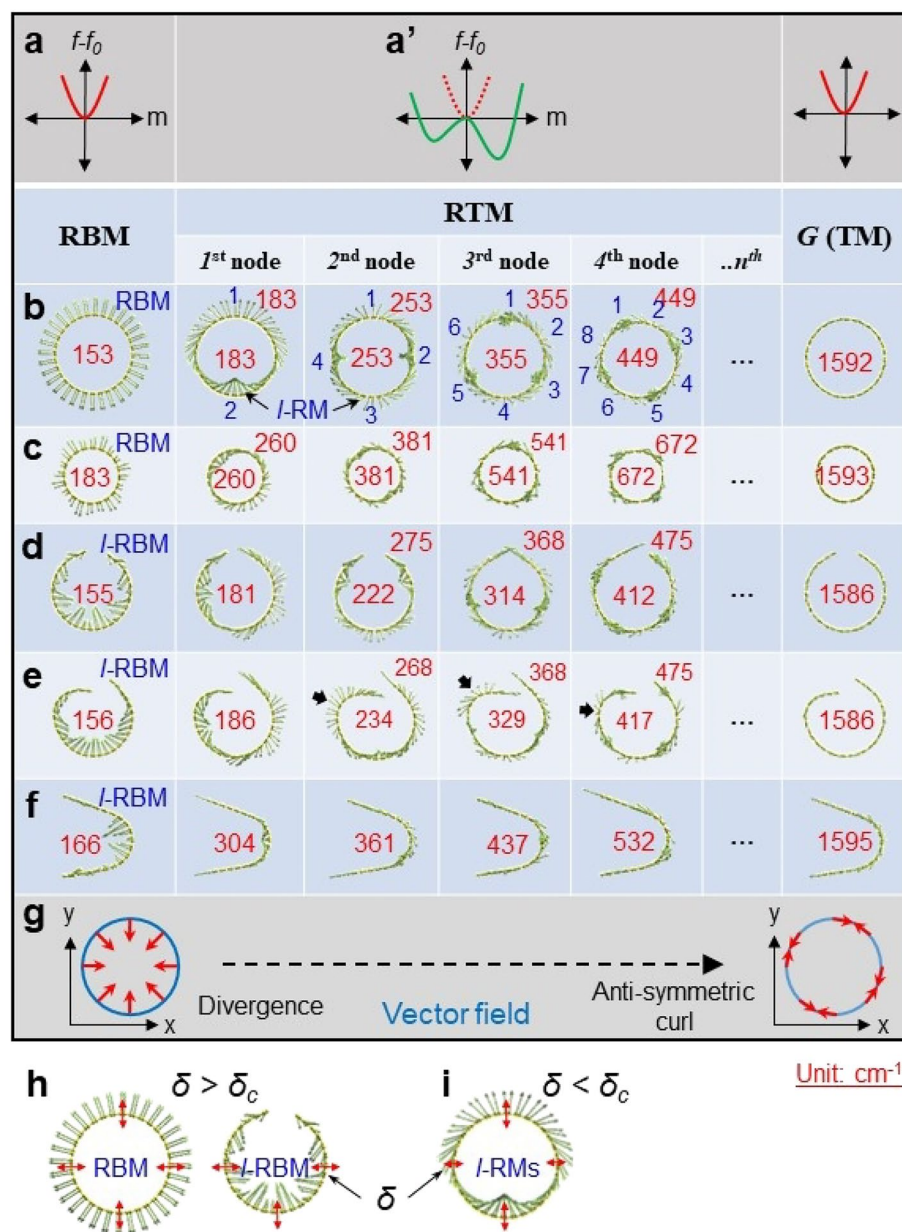


Figure 3. Simulated Raman-active modes for different graphene structures. (**a, a'**) Landau free energy landscape with one (**a**) or two minima (**a'**), which are the conditions of RBM (*I*-RBM) and *G*-mode or RTMs, respectively. (**b–f**), Raman modes simulated from concentric tubes of ~ 2.2 nm (**b**) and 1.4 nm (**c**) in diameter, opened tubes (**d,e**) and curved graphene (**f**), revealing RBM (or *I*-RBM), RTM and *G*-mode in order. We used the opened tubes instead of helical structures. The blue numbers represent the number of nodes for each RTM. The red numbers in (**b–f**) represent the frequencies of the modes. (**g**) Diagrams explaining divergence and anti-symmetric curl of vector fields. (**h, i**) Schematic explaining Landau condition for RBM ($\delta > \delta_c$) (**h**) and RTM ($\delta < \delta_c$) (**i**).

tendency of the RTMs with nodes (Fig. 3), we expect that the higher-frequency TM may dominate RTMs, and their intensity may gradually increase up to *G*-mode (which is contrary to the case of the lower-frequency RTMs below ~ 600 cm^{-1}), except for the *D* bands at 1319 and 1340 cm^{-1} .

The RBM peak at 149 cm^{-1} for Tuball-SWNTs corresponds to the diameters of ~ 2.2 nm on simulation (Fig. 3), which is at least $\sim 10\%$ overestimated, compared with the diameters measured to be 1.4–2.0 nm by HRTEM (Fig. 1). In this extension, we infer the weak peaks at 120 cm^{-1} and 137 cm^{-1} (in lower frequency than that of the RBM) corresponding to ~ 2.5 nm diameter to be from non-tubular carbon structures, *i.e.*, curved graphene¹⁴ with a curvature milder than the SWNTs of ~ 2.0 nm in diameter. Indeed, graphene structures coexist in the sample (Fig. 1b), and they can reveal *I*-RBM¹⁵ as well as RTMs when nano-curved (Fig. 3f).

We attribute two different Landau levels of RTMs for the opened tube structures (Fig. 3d and e) to the pseudo magnetic field. It has been reported that curved graphene produces a pseudo magnetic field due to strain^{40,41}.

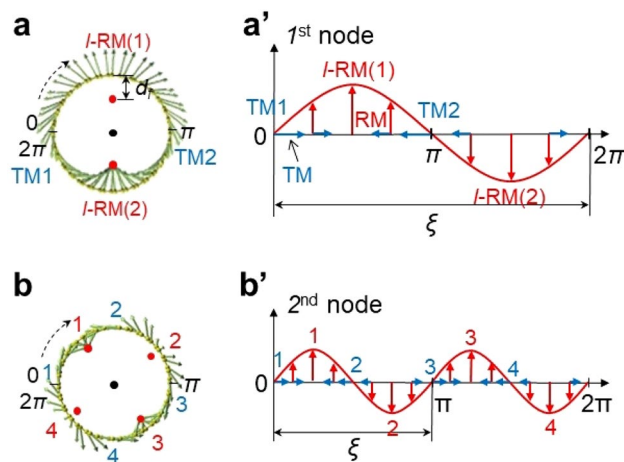


Figure 4. Conceptual explanation of RTMs and variation of depth of focus with node. (a, b) 1st and 2nd node RTMs for the concentric tube structure. The red solid dots indicate the decentered focus of Eigenvectors of I -RM. d_f is a depth of focus, the distance between the focus and the tube wall. The black dot in (a, b) indicates a focus of RBM where the depth of focus is r . (a', b') Sine curves of the RTMs where ξ is defined as a cycle of TM-RM-TM-RM-TM. Red and blue arrows indicate radial and transverse components deconvoluted from the slow varying Eigenvectors, respectively. Red and blue numbers in a-b' indicate the number of I -RM and I -TM, respectively.

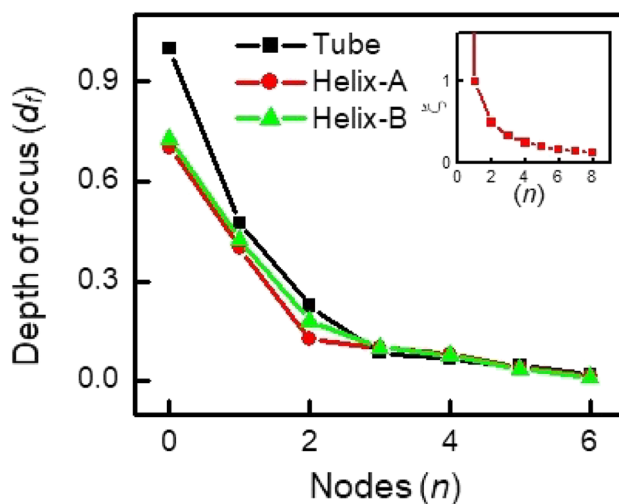


Figure 5. Variation of the depth of the focus of I -RMs with a node. Inset shows a variation of the coherence length with a node.

This may explain the inconsistent RTMs on the Raman spectra (Fig. 2), further supporting the helix model of SWNTs. A helical SWNT possesses dangling carbon atoms at the asymmetric helical edges³⁷, which break the rotational symmetry adding uneven strain to the system, resulting in diverse and inconsistent RTMs (Fig. 2b). Indeed, helical evidence is evident in Tuball-SWNTs (Fig. 1b) as well as arc-SWNTs²⁸. The helical edges are vulnerable to environmental conditions, bundled or individual and freestanding or deposited on a substrate, explaining further the diversity of the low-frequency Raman signals for SWNTs reported^{1–5,17–27}. The analysis may also explain the excitation wavelength dependence of the low-frequency Raman signals^{2,5,23–25} due to diverse curvatures of the helical edge (Supplementary Fig. 3), which can react differently with the energy range of the incident laser. Indeed, helical evidence of SWNTs, such as locally unrolled, twisted, or folded HRTEM morphologies, has been reported^{30–33}. We expect that the ordered optical transitions (~ 150 – 250 cm^{-1}) observed from 200 different isolated or bundled SWNTs reported by Paulo et al.⁶, the steplike dispersions (600 – 1100 cm^{-1}) observed from two different bundled samples (arc-SWNTs and HiPco) reported by Fantini et al.²³, as well as ZA-derived phonons (~ 400 , ~ 800 , and ~ 950 cm^{-1}) observed from highly aligned SWNTs reported by Vierck et al.²⁷ are the revelation of our Landau regulations of the RBMs and IFMs. Luo et al. also reported the steplike appearance of Raman signals in the energy range of 100 – 600 cm^{-1} observed from HiPco samples²⁴.

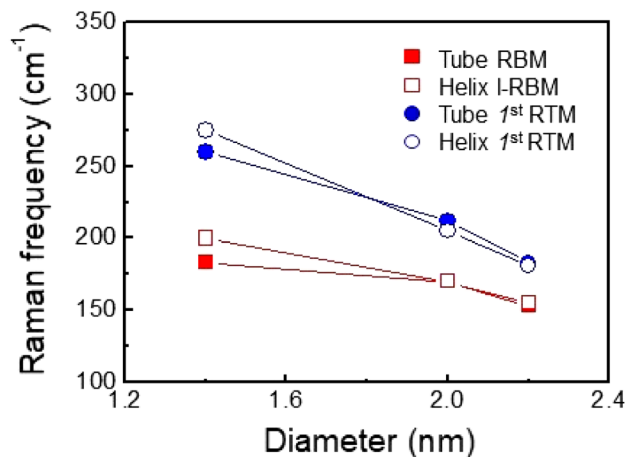


Figure 6. Simulated Raman frequency with the diameter of concentric and opened SWNTs. The data were obtained from the models with diameters of ~ 1.4 , ~ 2.0 , and ~ 2.2 nm (Supplementary Fig. 3).

We suggest the role of the RTMs interlinking the strongest G -mode and the 2nd strong RBM of SWNTs in a slowly varying manner. This explains the symmetric Raman spectra of SWNTs in intensity between the RBM and the G -mode^{1–5,19–27}. The spatial variation of the Eigenvectors on RTMs of SWNTs resembles the variation of vector fields from the divergence (comparable to RBM) to anti-symmetric curl (comparable to G -mode), as depicted in Fig. 3g. This suggests that our approach to Raman modes based on Landau theory can be extended to explain the transition of the vector field.

In summary, we manifested RTMs to be active Raman modes of SWNTs. They appear as ripple-like peaks between the RBM (~ 150 cm^{-1}) and the G -mode (1592 cm^{-1}), interlinking gradually. Our finding completes the analysis of the unique Raman spectrum for SWNTs where the ripple signals of SWNTs appearing at ~ 200 – 1440 cm^{-1} have been misinterpreted or disregarded for the last 30 years. The diversity of RBM and RTM peaks in shape and intensity (or absence) could be explained with the helix model of SWNTs, where the RBM becomes l -RBM. We propose that Landau theory can be a further way of understanding the nature of nanoscale matters with simple as well as powerful Raman analysis.

Method

TEM and Raman analysis. We analyzed two kinds of purified commercial SWNTs, Tuball (Oscial, Russia) and ASA-100F (arc-discharge, Hanwha Chemical, South Korea), where the purity is 80 wt% and 95 wt%, respectively. The impurity in Tuball samples includes metal nanoparticles as well as other carbonous structures (Fig. 1)³⁸. Raman measurements were carried out using Renishaw In-Via Raman Microscope with laser excitation of 532 nm, a spot size of 1–2 μm , laser power of 5 mW, and powder density of 1.6 $\text{mW}/\mu\text{m}^2$. Tuball samples were analyzed by Cs-corrected transmission electron microscope (Libra 200 HT Mc, Carl Zeiss). Earlier, we explored the arc-discharge sample as a helical structure with intensive high-resolution TEM observation²⁸.

Raman simulation. We carried out the simulation with concentric tubes ((10, 10), (15, 15), and (16, 16) tubes), opened tubes (without distortion), distorted opened tubes, as well as curved graphene. For the distorted opened tube structures, we mimicked the shape of the helical SWNTs³⁷. We used density functional theory (DFT) as implemented in the QUANTUM ESPRESSO simulation package⁴³. Generalized gradient approximation (GGA) was used for the exchange–correlation energy of electrons and ultra-soft pseudopotentials to represent the interaction between ionic cores and valence electrons⁴⁴. Kohn Sham wave functions were represented with a plane wave basis with an energy cutoff of 40 Ry, and a charge density cutoff of 240 Ry⁴⁵. Integration over the Brillouin zone (BZ) was sampled with a mesh of $1 \times 1 \times 2$ grid⁴⁶. Dynamical matrices at the Γ point ($q=0$) in BZ were computed using the perturbative linear response approach used in DFT (Fig. 6).

Data availability

The data that support the findings of the study are available in the public domain. However, the authors will be happy to discuss an appropriate accommodation for the reasonable request to J. L.

Received: 8 October 2022; Accepted: 21 March 2023

Published online: 27 March 2023

References

- Dresselhaus, M. S., Dresselhaus, G., Saito, R. & Jorio, A. Raman spectroscopy of carbon nanotubes. *Phys. Rep.* **409**, 47–99 (2005).
- Rao, A. M. *et al.* Diameter-selective Raman scattering from vibrational modes in carbon nanotubes. *Science* **275**, 187–191 (1997).
- Jorio, A. *et al.* Characterizing carbon nanotube samples with resonance Raman scattering. *New J. Phys.* **5**, 139 (2003).
- Hennrich, F. *et al.* Raman spectroscopy of individual single-walled carbon nanotubes from various sources. *J. Phys. Chem. B* **109**, 10567–10573 (2005).

5. Maultzsch, J., Telg, H., Reich, S. & Thomsen, C. Radial breathing mode of single-walled carbon nanotubes: Optical transition energies and chiral-index assignment. *Phys. Rev. B* **72**, 205438 (2005).
6. Araujo, P. T. *et al.* Third and fourth optical transitions in semiconducting carbon nanotubes. *Phys. Rev. Lett.* **98**, 067401 (2007).
7. Dresselhaus, M. S., Dresselhaus, G. & Saito, R. Physics of carbon nanotubes. *Carbon* **33**, 883–891 (1995).
8. Wang, J. J. *et al.* Free-standing subnanometer graphite sheets. *Appl. Phys. Lett.* **85**, 1265–1267 (2004).
9. Lui, C. H. *et al.* Observation of layer-breathing mode vibrations in few-layer graphene through combination Raman scattering. *Nano Lett.* **12**, 5539–5544 (2012).
10. Lin, M. L., Wu, J.-B., Liu, X.-L. & Tan, P.-H. Probing the shear and layer breathing modes in multilayer graphene by Raman spectroscopy. *J. Raman Spectrosc.* **49**, 19–30 (2018).
11. Podila, R., Rao, R., Tsuchikawa, R., Ishigami, M. & Rao, A. M. Raman spectroscopy of folded and scrolled graphene. *ACS Nano* **6**, 5784–5790 (2012).
12. Lui, C. H., Ye, Z., Keiser, C., Xiao, X. & He, R. Temperature-activated layer-breathing vibration in few-layer graphene. *Nano Lett.* **14**, 4615–4621 (2014).
13. He, R. *et al.* Observation of low energy Raman modes in twisted bilayer graphene. *Nano Lett.* **13**, 3594–3601 (2013).
14. Ramnani, P. *et al.* Raman spectra of twisted CVD bilayer graphene. *Carbon* **123**, 302–306 (2017).
15. Verzhbitskiy, I. A. *et al.* Raman fingerprints of atomically precise graphene nanoribbons. *Nano Lett.* **16**, 3442–3447 (2016).
16. Lee, J.-K. *et al.* Raman radial mode revealed from curved graphene. *J. Phys. Chem. Lett.* **8**, 2597–2601 (2017).
17. Journet, C. *et al.* Large-scale production of single-walled carbon nanotubes by the electric-arc-technique. *Nature* **388**, 756–759 (1997).
18. Rahmani, A., Sauvajol, J.-L., Rols, S. & Benoit, C. Nonresonant Raman spectrum in infinite and finite single-wall carbon nanotubes. *Phys. Rev. B Condens. Matter Mater. Phys.* **66**, 125404 (2002).
19. Anglaret, E. *et al.* Raman characterization of single wall carbon nanotubes prepared by the solar energy route. *Carbon* **12**, 1815–1820 (1998).
20. Dyke, C. A. & Tour, J. M. Solvent-free functionalization of carbon nanotubes. *J. Am. Chem. Soc.* **125**, 1156–1157 (2003).
21. Colomer, J.-F. *et al.* Characterization of single-wall carbon nanotubes produced by CCVD method. *Chem. Phys. Lett.* **345**, 11–17 (2001).
22. Dresselhaus, M. S. *et al.* Raman spectroscopy on isolated single wall carbon nanotubes. *Carbon* **40**, 2043–2061 (2002).
23. Fantini, C. *et al.* Steplike dispersion of the intermediate-frequency Raman modes in semiconducting and metallic carbon nanotubes. *Phys. Rev. B* **72**, 085446 (2005).
24. Luo, Z., Papadimitrakopoulos, F. & Doorn, S. K. Intermediate-frequency Raman modes for the lower optical transitions of semiconducting single-walled carbon nanotubes. *Phys. Rev. B* **75**, 205438 (2007).
25. Rao, R. *et al.* Double resonance Raman study of disorder in CVD-grown single-walled carbon nanotubes. *Carbon* **49**, 1318–1325 (2011).
26. Wang, J., Yang, J., Zhang, D. & Li, Y. Structure dependence of the intermediate-frequency Raman modes in isolated single-walled carbon nanotubes. *J. Phys. Chem. C* **116**, 23826–23832 (2012).
27. Vierck, A., Gannott, F., Schweiger, M., Zaumseil, J. & Maultzsch, J. *Carbon* **117**, 360–366 (2017).
28. Lee, J.-K. *et al.* Structure of single-wall carbon nanotubes: A Graphene helix. *Small* **10**, 3283–3290 (2014).
29. Meyer, R. R. *et al.* A composite method for the determination of the chirality of single walled carbon nanotubes. *J. Microsc.* **212**, 152–157 (2003).
30. Suenaga, K., Sato, Y., Liu, Z., Koshino, M. & Jin, C. HR-TEM of carbon network, Towards Individual CC bond imaging. *JEOL News* **44**, 32–37 (2009).
31. Hashimoto, A., Suenaga, K., Gloter, A., Urita, K. & Iijima, S. Direct evidence for atomic defects in graphene layers. *Nature* **430**, 870–873 (2004).
32. Bethune, D. S. *et al.* Cobalt-catalysed growth of carbon nanotubes with single-atomic-layer walls. *Nature* **363**, 605–607 (1993).
33. Terrones, M. Science and technology of the twenty-first century: synthesis, properties, and applications of carbon nanotubes. *Annu. Rev. Mater. Res.* **33**, 419–501 (2003).
34. Ge, M. & Sattler, K. Scanning tunneling microscopy of single-shell nanotubes of carbon. *Appl. Phys. Lett.* **65**, 2284–2286 (1994).
35. Wildöer, J. W. G., Venema, L. C., Rinzler, A. G., Smalley, R. E. & Dekker, C. Electronic structure of atomically resolved carbon nanotubes. *Nature* **391**, 59–62 (1998).
36. Marchand, M. *et al.* Growing a carbon nanotube atom by atom: “and yet it does turn”. *Nano Lett.* **9**, 2961–2966 (2009).
37. Park, Y. *et al.* Reinterpretation of single-wall carbon nanotubes by Raman spectroscopy. *J. Phys. Chem. C* **123**, 14003–14009 (2019).
38. Predtechenskiy, M. R. *et al.* New perspectives in SWCNT applications: Tuball SWCNTs. Part 1. Tuball by itself-All you need to know about it. *Carbon Trend* **8**, 100175 (2022).
39. Landau, L. D. & Lifshitz, E. M. *Statistical physics*, Pergamon Press (London) (1959).
40. Low, T. & Guinea, F. Strain-induced pseudomagnetic field for novel graphene electronics. *Nano Lett.* **10**, 3551–3554 (2010).
41. Castro-Villarreal, P. & Ruiz-Sanchez, R. Pseudomagnetic field in curved graphene. *Phys. Rev. B Condens. Matter Mater. Phys.* **95**, 125432 (2017).
42. He, M. *et al.* Growth modes and chiral selectivity of single-walled carbon nanotubes. *Nanoscale* **10**, 6744–6750 (2018).
43. Giannozzi, P. *et al.* QUANTUM ESPRESSO: A modular and open-source software project for quantum simulations of materials. *J. Phys. Condens. Matter* **21**, 395502 (2009).
44. Perdew, J. P., Burke, K. & Ernzerhof, M. Generalized gradient approximation made simple. *Phys. Rev. Lett.* **77**, 3865–3868 (1996).
45. Monkhorst, H. J. & Pack, J. D. Special points for Brillouin-zone integrations. *Phys. Rev. B Condens. Matter Mater. Phys.* **13**, 5188–5192 (1976).
46. Methfessel, M. & Paxton, A. T. High-precision sampling for Brillouin-zone integration in metals. *Phys. Rev. B Condens. Matter Mater. Phys.* **40**, 3616–3621 (1989).

Acknowledgements

This work was supported by KIST Future Resource Program (2E31011) and Korea Basic Science Institute Institutional Programs (D210400). The simulations were carried out by the server farm supercomputing facility at KIST.

Author contributions

K.H. performed a Raman simulation and realized that the low energy Raman modes of graphene structures, including SWNTs, follow Landau regulation. J.K. and S.L. performed a TEM analysis of SWNTs. J.P. analyzed Raman data. J. L. supervised the project. K.H. and J.L. analyzed the data and wrote the paper.

Competing interests

The authors declare no competing interests.

Additional information

Supplementary Information The online version contains supplementary material available at <https://doi.org/10.1038/s41598-023-32018-4>.

Correspondence and requests for materials should be addressed to J.-K.L.

Reprints and permissions information is available at www.nature.com/reprints.

Publisher's note Springer Nature remains neutral with regard to jurisdictional claims in published maps and institutional affiliations.



Open Access This article is licensed under a Creative Commons Attribution 4.0 International License, which permits use, sharing, adaptation, distribution and reproduction in any medium or format, as long as you give appropriate credit to the original author(s) and the source, provide a link to the Creative Commons licence, and indicate if changes were made. The images or other third party material in this article are included in the article's Creative Commons licence, unless indicated otherwise in a credit line to the material. If material is not included in the article's Creative Commons licence and your intended use is not permitted by statutory regulation or exceeds the permitted use, you will need to obtain permission directly from the copyright holder. To view a copy of this licence, visit <http://creativecommons.org/licenses/by/4.0/>.

© The Author(s) 2023